Unusual magnetic and transport properties in the Zintl phase $Eu_{11}Zn_6As_{12}$

Zhiyu Zhou ☉,[1] Ziwen Wang ☉,[1] Xiyu Chen ☉,[1] Jia-Yi Lu,[2] Junchao Zhang,[1] Xiong Luo,[1] Guang-Han Cao ☉,[2,3]
Shuai Dong,[1] and Zhi-Cheng Wang ☉[1,*]

[1]*Key Laboratory of Quantum Materials and Devices of Ministry of Education, School of Physics, Southeast University, Nanjing 211189, China*
[2]*School of Physics, Interdisciplinary Center for Quantum Information and State Key Laboratory of Silicon and Advanced Semiconductor Materials, Zhejiang University, Hangzhou 310058, China*
[3]*Collaborative Innovation Centre of Advanced Microstructures, Nanjing University, Nanjing 210093, China*

Narrow-gap rare-earth Zintl phases frequently exhibit fascinating physical phenomena owing to their various crystal structures, complex magnetic properties, and tunable transport behaviors. Here, we report the synthesis, magnetic, thermodynamic, and transport properties of a Eu-containing Zintl arsenide, $Eu_{11}Zn_6As_{12}$, which consists of infinite chains of Eu cations and anionic frameworks constructed from corner-sharing $ZnAs_4$ tetrahedra. $Eu_{11}Zn_6As_{12}$ exhibits complicated magnetic behavior owing to intricate exchange interactions mediated by the discrete anionic fragments. Two long-range magnetic transitions at 22 K (T_N) and 9 K (T^*), as well as exceptionally strong ferromagnetic fluctuations around 29 K (T_F), are indicated by the susceptibility, heat capacity, and resistivity measurements. Besides, $Eu_{11}Zn_6As_{12}$ displays metallic behavior, attributable to the hole carriers doped by slight Eu vacancies or the mixed valence of Eu^{2+} and Eu^{3+}. A prominent resistivity peak occurs around T_N, which is rapidly suppressed by the applied field, leading to a large negative magnetoresistance effect. A resistivity hysteresis is observed below 5 K, caused by a small net ferromagnetic component. Our study presents the distinct magnetic and transport properties of $Eu_{11}Zn_6As_{12}$, and further experiments are required to elucidate the origin of these behaviors. Moreover, our findings demonstrate that Eu-based Zintl phases are a fertile ground to study the interplay between magnetism and charge transport.

I. INTRODUCTION

Zintl phases, commonly known as valence-precise compounds consisting of electropositive cations and complex anionic frameworks, continue to attract significant research interest because of their diverse structures and physical properties, such as colossal magnetoresistance (CMR), thermoelectricity, anomalous Hall effect (AHE), and superconductivity [1–7]. Recently, multiple Eu-containing Zintl phases have been proposed as magnetic topological materials, including $EuSn_2As_2$, $EuMg_2Bi_2$, $EuIn_2As_2$, $EuCd_2As_2$, and $Eu_5In_2Sb_6$ [8–16]. Among these, the $CaAl_2Si_2$-type $EuCd_2As_2$ and its sibling compounds have garnered particular interest because of their various transport properties, tunable magnetism, and the strong interplay of magnetic ordering and band topology [17–20].

Previously, a Weyl semimetal state was identified in $EuCd_2As_2$ with the polarized spins of Eu [13–15,21,22]. Additionally, a CMR effect, attributed to strong magnetic fluctuations, was reported in the isostructural $EuCd_2P_2$, which rivals the manganates in the CMR magnitude [17,23,24]. Furthermore, the properties of the $CaAl_2Si_2$-type EuM_2X_2 ($M = Zn, Cd$; $X = P, As, Sb$) are extremely sensitive to carrier density in the material. For instance, $EuZn_2P_2$ could be transformed from an antiferromagnetic (AFM) insulator

to a ferromagnetic (FM) metal through the introduction of Eu vacancies during crystal growth [25]. Similarly, the magnetic ground states of other EuM_2X_2 have been successfully switched from AFM to FM ordering with a low carrier concentration [25–28]. These intriguing findings within EuM_2X_2 family underscore the rich phenomena and highly tunable properties in the magnetic Zintl phases with small band gaps, thereby motivating further exploration of Eu-containing Zintl phases with similar constituents and related structures.

In this paper, we present comprehensive characterizations of another Eu-based Zintl phase, $Eu_{11}Zn_6As_{12}$, which was previously synthesized but whose properties have not been reported [29]. $Eu_{11}Zn_6As_{12}$ is constructed from chains of Eu cations and anionic frameworks composed of corner-sharing $ZnAs_4$ tetrahedra. The MX_4 tetrahedron is also the basic structural fragment of EuM_2X_2. $Eu_{11}Zn_6As_{12}$ crystallizes in a $Sr_{11}Cd_6Sb_{12}$-type structure and displays complex magnetic behavior resulting from the competing AFM and FM interactions, with strong short-range FM fluctuations around 29 K (T_F), an AFM ordering at 22 K (T_N), and a third transition at 9 K (T^*). Moreover, $Eu_{11}Zn_6As_{12}$ exhibits metallic conductivity with a pronounced resistivity peak around T_N. The resistivity peak is suppressed rapidly in the field, leading to a large negative magnetoresistance (MR) effect near T_N. In addition, a small hysteresis in resistivity below 5 K is also noted, attributed to weakly FM magnetization for the uncompensated Eu spins. These features are absent in other Eu-containing 11-6-12 phases, such as $Eu_{11}Zn_6Sb_{12}$ and $Eu_{11}Cd_6Sb_{12}$ [30].

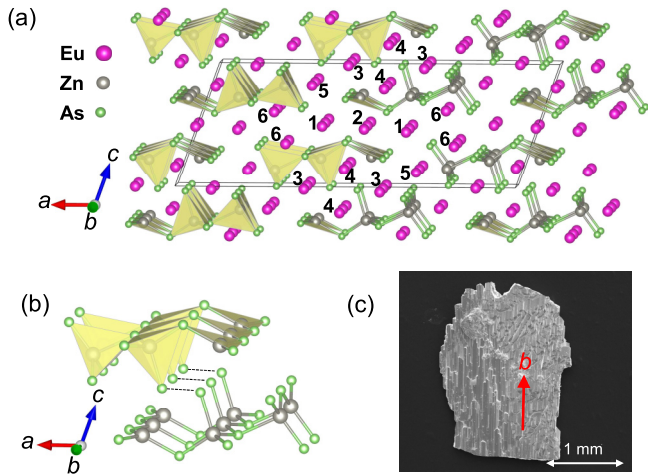
FIG. 1. (a) Combined polyhedral and ball-and-stick representations for the crystal structure of $Eu_{11}Zn_6As_{12}$. The $ZnAs_4$ tetrahedra is highlighted by faint yellow. Eu, Zn, and As atoms are shown as pink, gray, and green balls, respectively. The Eu sites are labeled with numbers. The structure of $Eu_{11}Zn_6As_{12}$ is viewed from the crystallographic c axis. Unit cell is outlined. (b) Further structural detail on $[Zn_6As_{12}]^{22-}$ networks in $Eu_{11}Zn_6As_{12}$. (c) A micrograph of single crystal of $Eu_{11}Zn_6As_{12}$.

Our findings underscore the surprising differences in the physical properties between these sister compounds, suggesting potential avenues for exploring unusual physical phenomena, such as the pronounced negative MR effect and nonlinear AHE, through full ionic substitution in narrow-gap rare-earth Zintl phases.

II. METHODS

A. Crystal growth

High-purity Eu pieces (99.999%), Zn powder (99.99%), and As lumps (99.99%) were used to grow single crystals of $Eu_{11}Zn_6As_{12}$ in Pb flux (99.999%). The Eu pieces were meticulously cleaned using a cutting plier to remove any oxides prior to use. All reagents and products were handled within an argon-filled glove box to prevent any potential oxidation or hydrolysis.

During an attempt to synthesize Eu_2ZnAs_2 with the Yb_2CdSb_2-type structure, we inadvertently obtained $Eu_{11}Zn_6As_{12}$ single crystals instead. The starting materials of Eu, Zn, As, and Pb, in a molar ratio of 2:1:2:30, were loaded into the alumina crucible with a total weight of 7 g. The crucible was sealed in an evacuated silica tube and heated directly to $1100\,°C$ over a period of 15 hours, then held at this temperature for 35 hours before being cooled down to $550\,°C$ at a rate of $3\,°C/h$. The silica tube was centrifuged and broken within the glove box. The products of $Eu_{11}Zn_6As_{12}$ crystals are predominantly lustrous platelets that appear to consist of transversely arranged, acicular-like single crystals [see Fig. 1(c)]. Nonetheless, isolated single crystals were still obtainable for structure determination and measurement purposes.

The $Eu_{11}Zn_6As_{12}$ samples are air-stable.

B. Structure determination

Suitable crystals were selected for single-crystal x-ray diffraction (SCXRD) analysis. Data collection was carried out at 150 K using a Bruker D8 Venture diffractometer, which was equipped with an IμS 3.0 Dual Wavelength system (Mo $K\alpha$ radiation, $\lambda = 0.71073$ Å) and an APEX-II CCD detector. The collected frames were reduced and corrected using the Bruker SAINT software suite. The crystal structure was determined using the intrinsic phasing method implemented in the SHELXT structure solution program within the Olex2 environment [31]. Subsequently, anisotropic refinements were performed with the SHELXL refinement package utilizing the least-squares method [32]. Finally, the crystal structure was visualized using the VESTA software [33]. Additionally, no twinning of the crystals was detected for our $Eu_{11}Zn_6As_{12}$ sample.

C. Magnetization, heat capacity, and resistivity measurements

The zero-field-cooling (ZFC) and field-cooling (FC) direct-current (dc) magnetization measurements of $Eu_{11}Zn_6As_{12}$ were conducted using a Magnetic Property Measurement System (MPMS 3, Quantum Design). The alternating-current (ac) susceptibility was collected on a Physical Property Measurement System (PPMS Dynacool, Quantum Design) with an ac measurement system (ACMS II). The temperature sweep rate is 2 K/min for the temperature-dependent magnetization measurements. The heat capacity measurement was also carried out on PPMS Dynacool with a relaxation-time technique. The transport measurements were performed on the TeslatronPT platform (Oxford Instruments) with a 12 T magnet, utilizing a custom-made probe coupled with an SR830 lock-in amplifier and 2400 meter (Stanford Research Systems). The magnetotransport data were measured with the current along the b axis (ρ_b) and the field perpendicular to it. High-quality single crystals were carefully selected and polished into the rectangular prism to facilitate resistivity calculations. Transport data were collected with a standard four-probe technique. Due to the practical limitation that only the crystallographic b axis can be distinguished, magnetic and resistivity data along the b axis and within the ac plane were collected, and the in-plane anisotropy was not explored.

D. First-principles calculations

Density functional theory (DFT) calculations were performed using the Vienna *ab initio* Simulation Package (VASP) [34]. Electron-ion interactions were described using projector augmented wave (PAW) pseudopotentials [35]. Because of the failure of density functionals in accurately describing partially filled $4f$ states, the PAW pseudopotentials were Eu_2, As, and Zn, as recommended by VASP. The plane-wave cutoff energy was set to 350 eV. The exchange-correlation functional was treated using the Perdew-Burke-Ernzerhof (PBE) parametrization of the generalized gradient approximation (GGA) [36]. A Γ-centered $1 \times 7 \times 3$ Monkhorst-Pack k mesh was used for Brillouin zone sampling. Both the lattice constants and atomic positions were fully optimized iteratively

TABLE I. Crystallographic data and refinement result of $Eu_{11}Zn_6As_{12}$ at 150 K.

Material	$Eu_{11}Zn_6As_{12}$
Crystal system	monoclinic
Space group	$C2/m$ (No. 12)
a (Å)	30.2522(18)
b (Å)	4.3256(2)
c (Å)	11.7518(5)
V (Å^3)	1447.44(13)
Z	2
ρ_{calc} (g/cm^3)	6.798
Temperature (K)	150
Radiation	Mo $K\alpha$
Reflections collected	16150
Independent reflections	1722
R_{int}	0.0871
Goodness-of-fit	1.115
R_1[a]	0.0339
wR_2[b]	0.0714

[a]$R_1 = \Sigma ||F_o| - |F_c||/\Sigma |F_o|$.

[b]$wR_2 = \left[\Sigma w \left(F_o^2 - F_c^2 \right)^2 / \Sigma w \left(F_o^2 \right)^2 \right]^{1/2}$.

until the total energy and the Hellmann-Feynman force on each atom converged to 10^{-6} eV and 0.05 eV/Å, respectively.

III. RESULTS AND DISCUSSION

A. Crystal structure

$Eu_{11}Zn_6As_{12}$ crystallizes in the monoclinic $Sr_{11}Cd_6Sb_{12}$-type structure (space group $C2/m$, No. 12), as shown in Fig. 1(a). The refined structure from SCXRD is listed in Table I. All cell dimensions of our crystal are 0.2% smaller than those reported in the literature, owing to the lower measurement temperature [29]. $Eu_{11}Zn_6As_{12}$ consists of Eu cations and covalently bonded polyanionic ribbons, formed through corner-sharing, which can be understood in the following way. Firstly, infinite chains of $^1_\infty[ZnAs_3]$ are formed by connecting ZnAs$_4$ tetrahedra along the crystallographic b axis. Then, two complete $^1_\infty[ZnAs_3]$ chains and a third incomplete $^1_\infty[ZnAs_2]$ chain, lacking a corner, integrate to constitute a polyanionic segment designated as $^1_\infty[Zn_3As_6]$. Two segments are then bridged through a As$_2$ dimer, giving rise to a subnetwork of $^1_\infty[Zn_6As_{12}]^{22-}$, illustrated in Fig. 1(b). And the interstitial spaces are occupied by the Eu cations. Note that three Eu chains (two of Eu1 and one of Eu2), situated at the center of the unit cell, are arranged linearly with uniform spacing owing to rotational symmetry. This configuration may facilitate the formation of FM domains, which will be addressed further in the discussion.

As mentioned in the METHODS section, attempts to synthesize Eu_2ZnAs_2 were unsuccessful, despite the existence of the Cd analog, Eu_2CdAs_2 [37]. The difference in radius between As and the transition metal Zn plays a crucial role in the final phase formation. Based on the existing Zintl phases Eu_2MX_2 and $Eu_{11}M_6X_{12}$ (M = Cd, Zn; X = P, As, Sb) [29,30,37,38], the trend is clear: the 2-1-2 phase (Yb_2CdSb_2-type) is favored when the radius of M is significantly larger

than that of X, whereas comparable radii or a smaller M favor the formation of the 11-6-12 phase.

B. Magnetic properties

$Eu_{11}Zn_6As_{12}$ exhibits a complicated magnetic behavior, which is summarized in Fig. 2. Panel (a) presents the dc susceptibility and inverse susceptibility of $Eu_{11}Zn_6As_{12}$ under $\mu_0H_{dc} = 0.1$ T. The anisotropy of $\chi_{\parallel b}(T)$ and $\chi_{\perp b}(T)$ is small. Notably, both $\chi_{\parallel b}(T)$ and $\chi_{\perp b}(T)$ increase obviously below 50 K. For $H \parallel b$, $\chi_{\parallel b}(T)$ keeps increasing at low temperatures and a kink at about 9 K is observed; while for $H \perp b$, $\chi_{\perp b}(T)$ deviates conspicuously from $\chi_{\parallel b}(T)$ around 18 K and becomes flat at 11 K, exhibiting a plateau-like behavior. Below 5 K, $\chi_{\perp b}(T)$ continues to increase and almost catches up with $\chi_{\parallel b}(T)$ at 1.8 K. By fitting the $\chi(T)$ data from 150 to 300 K to the Curie-Weiss law $\chi(T) - \chi_0 = C/(T - \theta)$, a Weiss temperature of $\theta \approx 32$ K and an effective moment of $\mu_{eff} \approx 7.6 \mu_B$/Eu are obtained. The positive θ is indicative of strong FM interaction in $Eu_{11}Zn_6As_{12}$. μ_{eff} of $Eu_{11}Zn_6As_{12}$ is a bit lower than the theoretical value of 7.94 μ_B for Eu^{2+}, may suggest the possibility of a slightly mixed valence of Eu^{2+} and Eu^{3+} or a small proportion of Eu vacancies. The comparatively low μ_{eff} is consistent with the saturation magnetizations (M_{sat}) shown in Fig. 2(d), which are also slightly below the theoretical M_{sat} of 7 μ_B.

The temperature-dependent derivatives of susceptibility ($d\chi_{dc}/dT$) are plotted in Fig. 2(b) to exhibit the features related to the magnetic transitions. A negative peak is situated at 27 K, corresponding to the rise below 50 K in Figs. 2(a) and 2(c). Generally, the rapid rise in susceptibility indicates the presence of FM correlations, which is confirmed by a small bifurcation of the ZFC and FC data under a small field of 50 Oe in Figs. 2(c) and 7(c), as well as the large out-of-phase contribution of ac susceptibility ($\chi''_{ac} \sim 7\%\chi'_{ac}$) below 29 K, as shown in Figs. 2(e) and 2(f). However, it is more appropriate to regard the transition around 27 K as a sign of short-range FM fluctuations rather than the establish of long-range FM order based on the following observations: (i) The signature of transition around 27 K is absent in the temperature-dependent specific heat (C_p) in Fig. 3(a), although a weak rise in C_p/T from 28 K is seen in Fig. 3(c); (ii) the magnetic anisotropy of susceptibility in Figs. 2(a) and 2(c) is slight, unlike a typical ferromagnet; (iii) the splitting of ZFC and FC data in Fig. 2(c) is rather small; and (iv) the rise of susceptibility around 27 K is unremarkable, unlike other reported Eu-based ferromagnets [3,25–28]. One may note that the χ''_{ac} peak for the fluctuations slightly shifts to higher temperature by about 0.6 K when the frequency increases from 100 Hz to 9984 Hz, which does not indicate a glassy behavior, since weak frequency dependence can also be observed when FM phase appears [39]. Moreover, we define the temperature of the $d\chi''_{ac}/dT$ minimum or the χ''_{ac} onset, i.e., 29 K, as the characteristic temperature (T_F) of FM fluctuations.

The first long-range order occurs around 22 K, as evidenced by the plateau in Fig. 2(c) and the small peaks of χ_{ac} in Figs. 2(e) and 2(f). This transition is not conspicuous for $\chi_{dc}(T)$ in Fig. 2(a); only a small kink is visible from $d\chi_{dc}/dT$ in Fig. 2(b). Nonetheless, this transition should be considered as a long-range order given the evident changes of heat
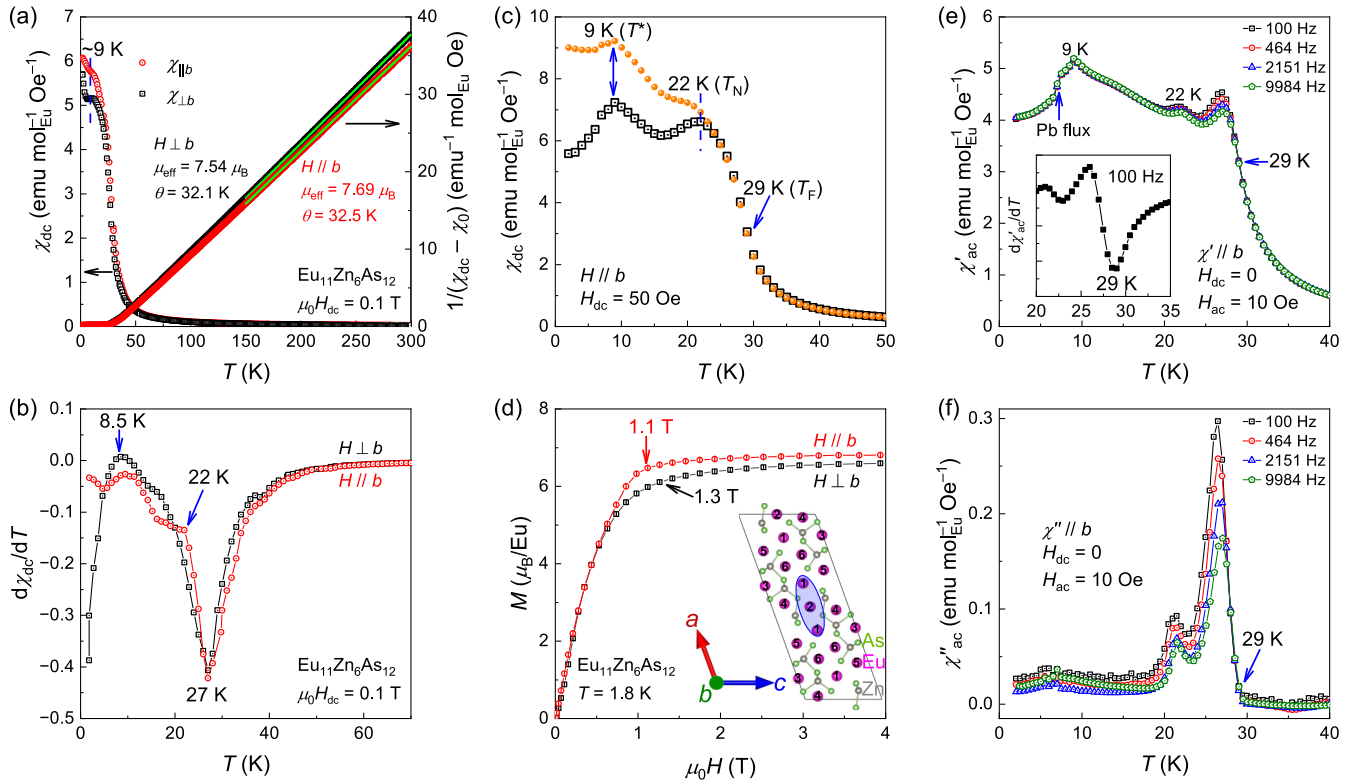
FIG. 2. (a) Susceptibility (left axis) of $Eu_{11}Zn_6As_{12}$ and the Curie-Weiss analysis (right axis). Red circles and black squares represent $\chi(T)$ along and perpendicular to the b axis, respectively. The corresponding Curie-Weiss fit is plotted as the green line on the reciprocal of susceptibility. (b) $d\chi/dT$ as a function of temperature to show the magnetic transitions of $Eu_{11}Zn_6As_{12}$. (c) The bifurcation of ZFC (black) and FC (orange) data collected under a field of 5 mT along the b axis. (d) Magnetization of $Eu_{11}Zn_6As_{12}$ as a function of fields along (red circles) and perpendicular to (black squares) the b axis. Inset shows a projection of $Eu_{11}Zn_6As_{12}$ structure along [010] direction and highlights the Eu1 and Eu2 sites. (e) The in-phase component of ac magnetic susceptibility $\chi'(T)$ at different frequencies. The ac driving amplitude was 10 Oe and the dc magnetic field is zero. Inset displays the $d\chi'/dT$ as a function of T. (f) The out-of-phase component of ac magnetic susceptibility $\chi''(T)$ at different frequencies.

capacity and resistivity close to the corresponding temperature, which will be discussed later. The long-range order is likely AFM since $\chi_{dc}(T)$ does not show a sudden increase below 22 K. It is worth noting that the typical decline in $\chi_{dc}(T)$ resulting from the AFM transition is subtle, not only caused by the strong background from FM fluctuations mentioned earlier, but also because of the low-dimension magnetic correlations arising from the chain-like structure of $Eu_{11}Zn_6As_{12}$. It is common to observe the absence of a sharp transition peak for quasi-one-dimensional or quasi-two-dimensional antiferromagnets [40–42]. Additionally, the presence of a χ''_{ac} peak around 22 K, which is typically absent in AFM materials, can be attributed to the background FM fluctuations and the fact that only the spins at partial Eu sites are aligned antiparallelly. Hence, the AFM transition temperature (T_N) of $Eu_{11}Zn_6As_{12}$ is 22 K according to the susceptibility criteria.

A clear transition peak at 9 K is observed for both dc susceptibility (ZFC and FC) in Fig. 2(c) and in-phase ac susceptibility χ'_{ac} in Fig. 2(e). Considering the evident heat capacity jump at 8.5 K in Fig. 3(a), we believe this is a bulk transition resulting from the spin reorientation or the ordering of the remaining portion of Eu sites. Moreover, this transition seems to be AFM since the response of χ''_{ac} around 9 K almost vanishes. The intricate magnetic behavior of $Eu_{11}Zn_6As_{12}$ could be ascribed to its complex crystal

structure. Given the predominant FM interaction indicated by the positive Weiss temperature, it is plausible to assume FM coupling along the Eu chains for the higher susceptibility and magnetization along the b axis. Moreover, for $Eu_{11}Zn_6As_{12}$, three Eu atoms (Eu1-Eu2-Eu1) are arranged linearly (bond angle 180°) in [010] plane with a distance ($d_{Eu1-Eu2}$) of 3.736 Å, as highlighted in the inset of Fig. 2(d). The distance is much shorter than the Eu-Eu distance (4.326 Å) along the Eu chain (b axis) and the in-plane Eu-Eu distances of many other Eu-based layered materials ($4 \sim 5$ Å) [19,22], which may favor the FM coupling for the enhanced exchange interaction and dipolar interaction [43,44]. Therefore, it is reasonable to suppose a FM coupling between Eu1 and Eu2 chains of $Eu_{11}Zn_6As_{12}$. The interchain FM coupling may exist not only between Eu1 and Eu2, but also between chains of Eu1-Eu5 ($d_{Eu1-Eu5} = 3.711$ Å, Eu5-Eu1-Eu2 bond angle 107.6°). The ferromagnetically coupled Eu chains are coupled through the AFM interactions mediated by the network of $\frac{1}{\infty}[Zn_6As_{12}]$. However, because of the crooked anionic segments, perfect compensation of ferromagnetically coupled units may be difficult, resulting in a small net magnetization that leads to the splitting of the ZFC and FC data below T_F for both $H \parallel b$ and $H \perp b$ [see Fig. 7(c)], as well as the resistivity hysteresis near zero temperature in Fig. 4. Moreover, the spins of Eu may order progressively owing to the
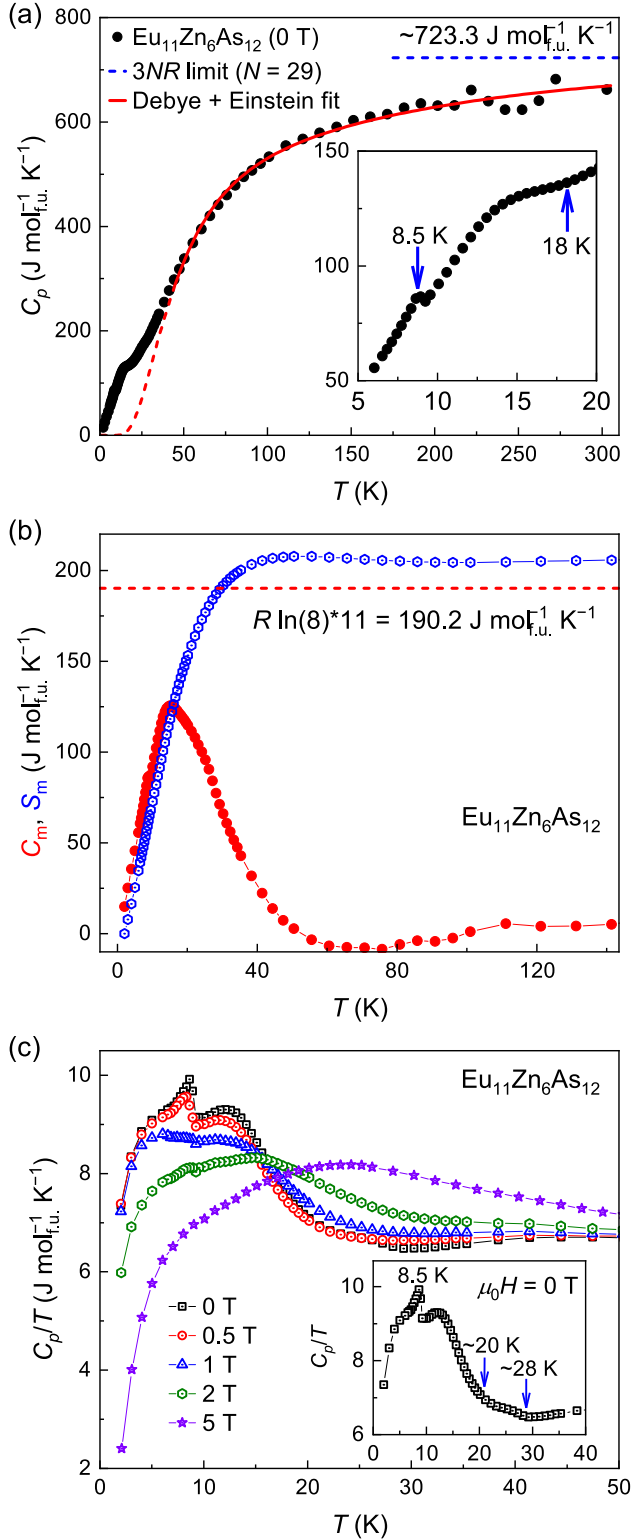
FIG. 3. (a) Temperature dependence of zero-field heat capacity, $C_p(T)$, along with a fit from 45 to 300 K by a combination of the Debye and Einstein models (red curve). Inset zooms in the $C_p(T)$ data below 20 K to highlight the transitions. (b) Magnetic heat capacity $C_m(T)$ (red dots) and entropy $S_m(T)$ (blue circles) calculated from $C_m(T)$, plotted as a function of temperature. The red-dashed line marks the magnetic entropy expected for Eu^{2+} ions. (c) C_p/T vs T under various magnetic fields. Inset plots zero-field C_p/T vs T individually to show the transitions.

varied exchange interactions between the multiple magnetic Wyckoff sites. Hence, it is also possible that the three magnetic transitions occur on different Eu sites at successive temperatures.

By comparison, $Eu_{11}Zn_6Sb_{12}$ and $Eu_{11}Cd_6Sb_{12}$, the sibling compounds of $Eu_{11}Zn_6As_{12}$, are nonmagnetic or clearly AFM, and their Weiss temperature are below 0 K [30]. The sharp contrast is attributed to the obviously longer Eu-Eu distances in the antimonides, including the intra- ($\gtrsim 4.5$ Å) and interchain ($\gtrsim 3.9$ Å) distances. Of course, further experiments, such as neutron scattering, are necessary to determine the magnetic structure of $Eu_{11}Zn_6As_{12}$.

C. Heat capacity

To confirm the magnetic transitions of $Eu_{11}Zn_6As_{12}$ revealed by the magnetization data, we measured the specific heat (C_p) and present the result in Fig. 3. As shown in Fig. 3(a), the C_p value at room temperature is smaller than the expected Dulong-Petit limit of 723.3 J $mol_{f.u.}^{-1}$ K^{-1} ($N = 29$) for $Eu_{11}Zn_6As_{12}$. In the lower-right inset, a broad hump attributed to the AFM transition is observed below 18 K, corresponding to the resistivity peak at this temperature and slightly lower than the T_N value determined by the susceptibility. The C_p of $Eu_{11}Zn_6As_{12}$ around T_N does not exhibit a λ-type peak, consistent with its structure of infinite chains, since the λ-type peak is typically absent in materials with low-dimensional AFM correlations [40,45]. With decreasing temperature, a small but clear anomaly occurs at 8.5 K, corresponding to the second bulk transition (T^*) discussed earlier. We fit the zero-field C_p data from 45 to 300 K by a combination of the Debye and Einstein models according to

$$C_p(T) = \alpha C_D(T) + (1 - \alpha)C_E(T), \qquad (1)$$

where

$$C_D(T) = 9NR\left(\frac{T}{\Theta_D}\right)^3 \int_0^{\Theta_D/T} \frac{x^4 e^x}{(e^x - 1)^2}dx, \qquad (2)$$

$$C_E(T) = 3NR\left(\frac{\Theta_E}{T}\right)^2 \frac{e^{\Theta_D/T}}{(e^{\Theta_D/T} - 1)^2}. \qquad (3)$$

Here, $C_D(T)$ and $C_E(T)$ represent the lattice contributions from the Debye and Einstein models, respectively. Θ_D and Θ_E are the Debye temperature and Einstein temperature, and α determines the relative contributions of the Debye and Einstein components. The fitted parameters are $\Theta_D = 1025.1$ K, $\Theta_E = 140.6$ K, and $\alpha = 0.15$.

With the fitted data, the magnetic contribution to the heat capacity (C_m) was obtained by subtracting the lattice contribution, and the magnetic entropy (S_m) was calculated by the integral

$$S_m(T) = \int_0^T \frac{C_m(T)}{T}dT, \qquad (4)$$

which are plotted in the Fig. 3(b). The resultant S_m is about 205 J $mol_{f.u.}^{-1}$ K^{-1}, slightly exceeding the expected value of $S_m = 11R\ln(2S + 1)$ with $S = 7/2$. This excess may be attributed to an overestimation of the Einstein component because of the data fluctuation above 200 K. Additionally, the
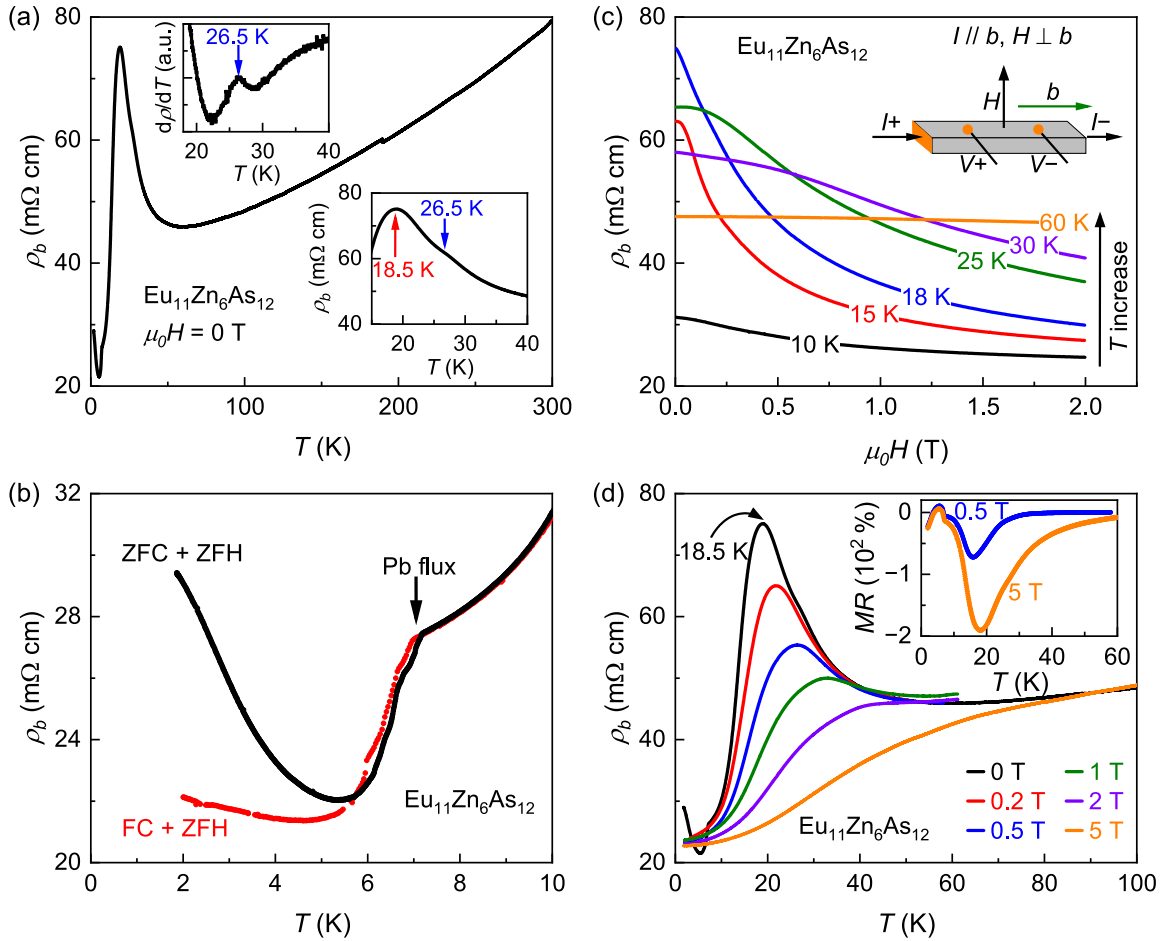
FIG. 4. (a) Temperature-dependent electrical resistivity of $Eu_{11}Zn_6As_{12}$ along the b axis. The upper-left inset shows the derivative of $\rho_b(T)$, while the lower-right inset zooms in $\rho_b(T)$ to show the transitions. (b) The hysteresis of $\rho_b(T)$. The black dots represent the data measured in zero-field-heating (ZFH) process after cooling to 2 K without the field (ZFC), and the red dots represent the data measured in ZFH process after cooling to 2 K under 5 T (FC). (c) Field-dependent ρ_b at various temperatures from 10 to 60 K. Inset illustrates the electrode configuration for the resistivity measurement. (d) Temperature-dependent ρ_b with applied magnetic field of 0, 0.2, 0.5, 1, 2, and 5 T. Inset shows the MR as a function of temperature at 0.5 and 5 T.

evident contributions to $C_m(T)$ and $S_m(T)$ above T_N arise from short-range magnetic interactions.

Figure 3(c) shows the C_p/T data under several magnetic fields. The sharp peak at 8.5 K confirms the bulk transition at T^*. The broad shoulder below T^* is commonly observed in $S = 7/2$ magnets [44,46]. Furthermore, as shown in the inset, two successive rises are observed starting around 28 K and 20 K, contributed by the magnetic fluctuations around T_F and AFM ordering at T_N, respectively. Upon applying the fields, the peak at T^* is suppressed and disappears substantially above 2 T. Moreover, the phase transitions at T_N and T_F are severely broadened by the fields, resulting in a weight shift of heat capacity from lower to higher temperature.

D. Magnetotransport

$Eu_{11}Zn_6As_{12}$ exhibits distinct electrical transport properties from the isostructural $Eu_{11}Cd_6Sb_{12}$ and $Eu_{11}Zn_6Sb_{12}$, which were reported to show simple metallic behavior [30]. The electrical resistivity along the b axis [$\rho_b(T)$] of $Eu_{11}Zn_6As_{12}$ under zero field is presented in Fig. 4(a). It

shows a mild decrease with decreasing temperature above 50 K and reveals a large peak at 18.5 K, slightly lower than T_N based on susceptibility criteria. Below the transition, $\rho_b(T)$ drops rapidly for the reduced magnetic scattering. $\rho_b(T)$ is higher than 20 mΩ cm across the entire temperature range, significantly above the resistivity of $Eu_{11}Cd_6Sb_{12}$ [30]. This is attributed to the less orbital hybridization in $Eu_{11}Zn_6As_{12}$ because of the smaller spatial extension of the Zn and As orbitals. The magnified view of $\rho_b(T)$ between 15 and 40 K is shown in the lower-right inset. A weak hump around 26.5 K is seen, consistent with the temperature range of susceptibility rise in Figs. 2(a) and 2(c). To highlight the resistivity anomaly, we plot the temperature derivative of $\rho_b(T)$, $d\rho/dT$, in the upper-left inset. An explicit peak is observed at 26.5 K, consistent with the characteristic temperature of FM fluctuations indicated by the susceptibility.

The zero-field resistivity of $Eu_{11}Zn_6As_{12}$ at low temperatures is affected by the remanent magnetization, i.e., depends on the processing history in the field, manifested in the Fig. 4(b). Both the black and red dots were measured via zero-field-heating (ZFH) process, and the distinction is that

the red data was collected following cooling the sample to 2 K in a field of 5 T, whereas the black data was collected without subjecting the sample to any magnetic field treatment. Both ZFC and FC data drop at 7 K, resulting from a small Pb-flux residue on the rugged surface. The evident upturn in the ZFC resistivity is attributed to the magnetic scattering arising from the uncompensated Eu spins. Conversely, the FC data exhibit no substantial increase, as the spins are aligned in the applied magnetic field. The bifurcation between ZFC and FC data validates the existence of the net FM component under low temperatures.

By applying the magnetic field, $Eu_{11}Zn_6As_{12}$ shows a noticeable negative MR effect, as presented in Figs. 4(c) and 4(d). $\rho_b(H)$ was measured with the field parallel to the ac plane ($H \perp b$). At 60 K, no conspicuous MR effect is observed below 2 T. With the decreasing temperature, the negative MR is enhanced by the strong magnetic fluctuations above the AFM order, and reaches a maximum at T_N of 18 K. At 18 K, ρ_b declines by 60% under the field of 2 T. Below T_N, the MR effect is diminished gradually for the reduction of spin-dependent scattering. The temperature-dependent ρ_b at various fields are also depicted in Fig. 4(d). Note that the tail of $\rho_b(0\,T)$ at low temperatures is absent for the curves with field, because both the superconductivity of Pb and magnetic scattering are suppressed by the magnetic field. The resistivity peak at 18.5 K is suppressed rapidly in the field, resulting in a maximum MR of −190% at 5 T, with the definition that $MR = 100\% \times [\rho(H) - \rho(0)]/\rho(H)$. The calculated MR at 0.5 T and 5 T are plotted as a function of temperature in the inset of Fig. 4(d). Note that the small positive MR at low temperatures results from the suppression of the superconductivity of Pb, not the intrinsic behavior of $Eu_{11}Zn_6As_{12}$.

E. Hall effect

The field dependence of the Hall resistivity (ρ_{xy}) for $Eu_{11}Zn_6As_{12}$ is shown in Fig. 5(a), with $I \parallel b$ and $H \perp b$. At $T = 60$ K, ρ_{xy} depends on the field linearly with a positive slope of 5.2 $\mu\Omega$ cm T^{-1}, indicating that ρ_{xy} is dominated by the ordinary Hall effect (OHE) when temperature is well above T_N. The carriers are identified as hole type with the density of $n = 1.2 \times 10^{20}$ cm^{-3} based on the slope of $\rho_{xy}(H)$. Under a high field (>4 T), all $\rho_{xy}(H)$ curves follow a slope similar to the curve at 60 K, suggesting an almost constant carrier density in $Eu_{11}Zn_6As_{12}$. As the temperature gets closer to 18 K, the curves become more and more nonlinear, which is contributed by the AHE. At 18 K, a small peak is observed at approximately 0.26 T, suggesting the presence of a nonlinear component in addition to the conventional AHE contribution that is proportional to the magnetization.

We analyzed the nonlinear AHE for the data at 15, 18, and 25 K, as shown in Fig. 5(b). The total Hall resistivity can be expressed as a sum of three parts, $\rho_{xy} = R_0\mu_0H + R_S M + \rho_{xy}^{NL}$, where $R_0\mu_0H$ and $R_S M$ represent the OHE and conventional AHE contributions, respectively. The third term, ρ_{xy}^{NL}, is not proportional to either μ_0H or M and represents the nonlinear AHE. The magnetization at these temperatures varies mildly at high fields and can be taken as a constant value. The $M(H)$ curves at related temperatures are presented in Fig. 7(b) in the Appendix. Therefore, $R_0\mu_0H + R_S M$ is only dependent
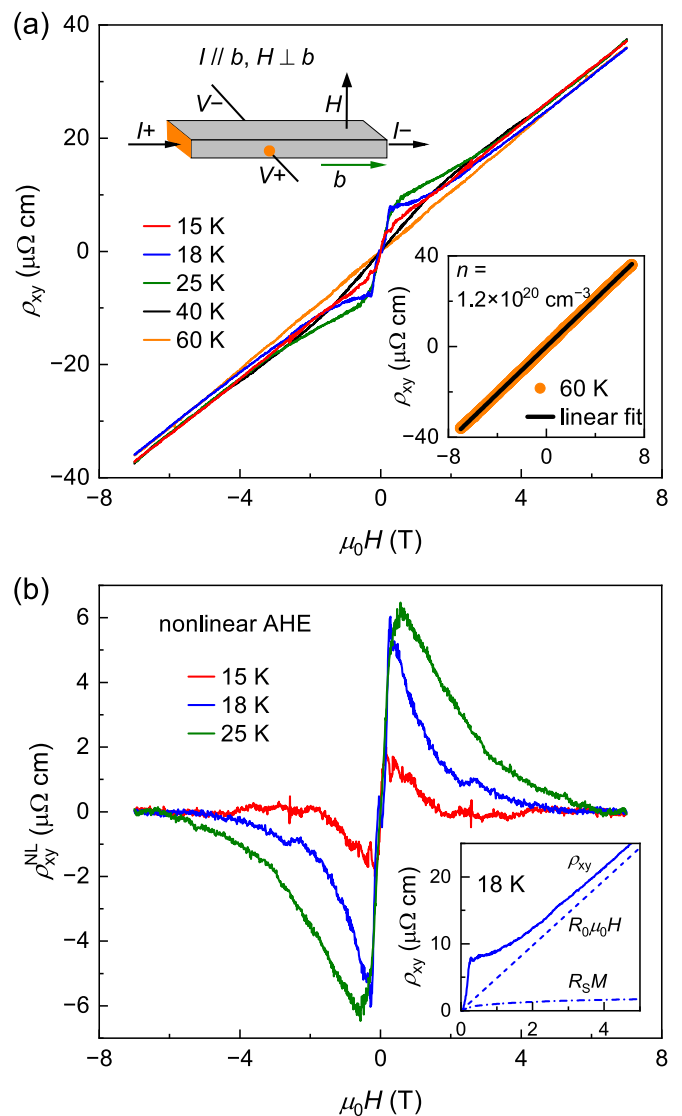

FIG. 5. (a) Magnetic field dependence of the Hall resistivity of $Eu_{11}Zn_6As_{12}$ at several temperatures. The fields are applied perpendicular to the b axis while the current is along the b axis, as illustrated in the upper left schematic. Lower-right inset shows a linear fit for the Hall resistivity at 60 K. (b) Extracted nonlinear AHE contribution from Hall resistivity at 15 K, 18 K, and 25 K. Inset shows the decomposition of $\rho_{xy}(H)$ at 18 K, where the total ρ_{xy}, OHE contribution, and conventional AHE contribution are plotted as solid, dashed, dash-dotted lines, respectively.

on μ_0H at high fields. We fit the total Hall resistivity $\rho_{xy}(H)$ from 6 T to 7 T to the equation $R_0\mu_0H + R_S M$, where R_0 is the resulting slope, and R_S could be obtained from the intercept $R_S M$. Thus, the nonlinear AHE could be obtained by subtracting OHE and conventional AHE. The decomposition of ρ_{xy} at 18 K is presented in the inset of Fig. 5(b). The extracted ρ_{xy}^{NL} strongly depends on the temperature and field, exhibiting a clear peak for the $\rho_{xy}^{NL}(H)$ curves. For the 25 K curve, ρ_{xy}^{NL} achieves its maximum amplitude at 0.6 T, which constitutes 62% of the total Hall resistivity ($\rho_{xy}^{NL}/\rho_{xy} = 0.62$). Similar phenomena of large nonlinear AHE contributions have also been reported in other Eu-based Zintl compounds, specifically
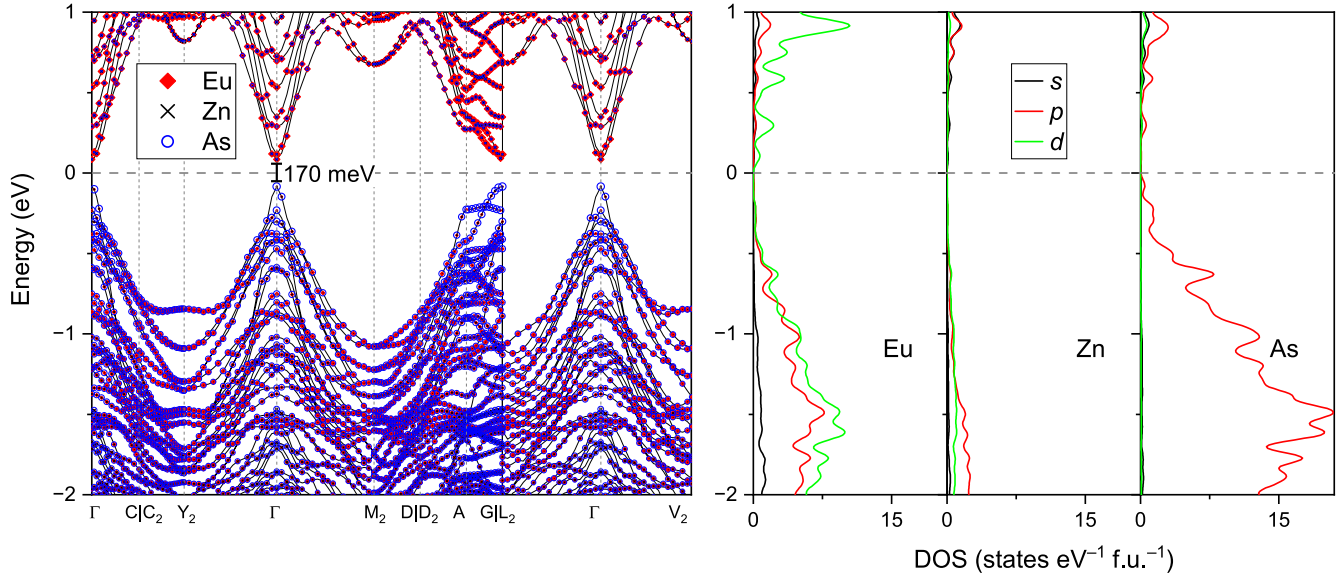
FIG. 6. Band structure and DOS of $Eu_{11}Zn_6As_{12}$, calculated by treating the Eu $4f$ electrons as core states.

EuM_2X_2 (M = Zn, Cd; X = P, As, Sb) [18,47,48], which are believed to originate from nontrivial band topology or nonzero spin chirality within the domain walls [15,48,49]. Given the strong FM fluctuations indicated by the magnetic data in Fig. 2, it is not surprising that potentially existing noncollinear spin configurations between the domains host local magnetic chirality and drive the nonzero Berry curvature. The nonlinear AHE contribution diminishes gradually below T_N, as demonstrated by weak ρ_{xy}^{NL} contribution at 15 K.

If the hole carriers in $Eu_{11}Zn_6As_{12}$ are considered to arise from slight Eu defects, the density of Eu vacancies is estimated to be 0.087 per formula unit (or 0.174 hole/f.u.) given $n = 1.2 \times 10^{20}$ cm^{-3}. That is to say, the proportion of Eu vacancies to all Eu sites is 0.8%. It is common to see large p-type carrier concentrations in Zintl phases for the cation defects, such as the widely studied thermoelectric materials AZn_2Sb_2 (A = Ca, Sr, Eu, Yb) [50,51]. Actually, the formation of cation vacancies is energetically favorable in the cation-rich Zintl phases, such as the 11-6-12 phase [52]. Compared to $Eu_{11}Zn_6Sb_{12}$ and $Eu_{11}Cd_6Sb_{12}$, the smaller unit

cell of $Eu_{11}Zn_6As_{12}$ signifies the higher concentration of Eu, implying a higher possibility of Eu vacancies. In addition, recent studies on EuM_2X_2 (M = Cd, Zn; X = P, As) have revealed that FM interaction between Eu layers could be induced or enhanced by the hole carriers [25]. Hence, the carriers in $Eu_{11}Zn_6As_{12}$ may not only account for the metallic behavior, but also be responsible for its enhanced FM coupling.

The origin of carriers in $Eu_{11}Zn_6As_{12}$ can also be explained in light of the mixed valence of Eu^{2+} and Eu^{3+}. A previous study comprehensively discussed the complex chemical bonding and charge balance of the isostructural Zintl compounds, $Sr_{11}Cd_6Sb_{12}$ and $Ba_{11}Cd_6Sb_{12}$, affirming that these materials conform to the Zintl concept [53]. However, this analysis may not be applicable to rule out the mixed valence in $Eu_{11}Zn_6As_{12}$. For example, $EuNi_2P_2$ is a mixed-valent compound [54], distinct from its siblings with divalent alkaline-earth elements, $SrNi_2P_2$ and $BaNi_2P_2$ [55,56]. The combination of 9 Eu^{2+} and 2 Eu^{3+} could generate a carrier concentration of 0.18 hole/f.u., which is excellently consistent with
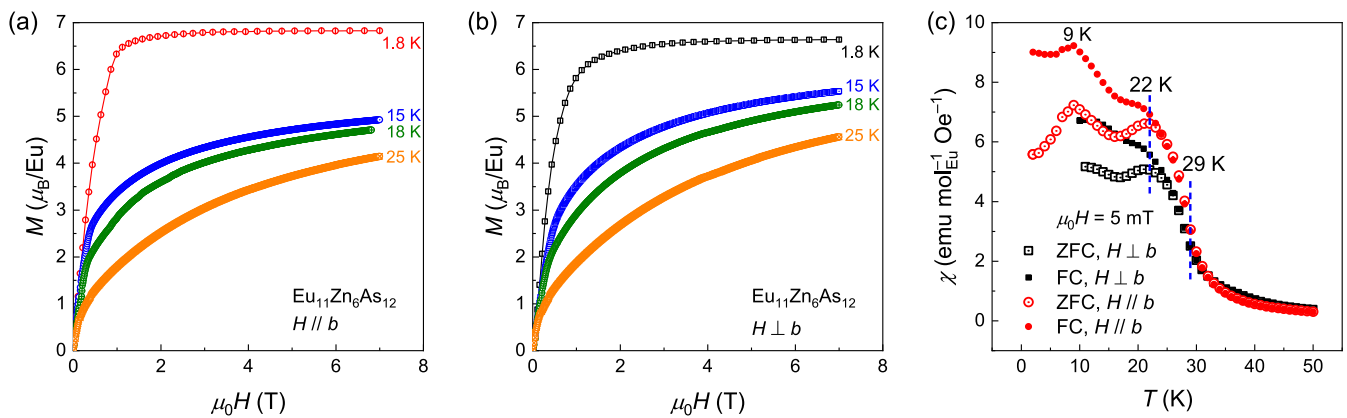

FIG. 7. [(a), (b)] Anisotropic magnetization of $Eu_{11}Zn_6As_{12}$ at 1.8, 15, 18, and 25 K, as a function of fields (a) along and (b) perpendicular to the b axis. (c) Anisotropic ZFC and FC curves under a field of 5 mT.

the value resulting from the Hall effect. Nevertheless, considering that the discrepancies between the experimental and theoretical values of μ_{eff} and M_{sat} are not conspicuous, some electrons may transfer from As $4p$ orbitals to Eu $4f$ orbitals, not changing the hole density but reducing the ratio of Eu^{3+}.

Both assumptions, the presence of Eu vacancies in the lattice and the mixed valence of Eu^{2+} and Eu^{3+}, make sense to elucidate the metallic behavior in $Eu_{11}Zn_6As_{12}$. However, further experiments are necessary to verify these assumptions.

F. DFT calculations

To gain deeper insight into the electronic properties, we conducted DFT calculations for $Eu_{11}Zn_6As_{12}$. However, attempts to treat the half-filled $4f$ electrons of Eu^{2+} ($4f^7$) as valence electrons failed to converge. Generally, partially filled $4f$ states cannot be accurately described by current density functionals because of self-interaction errors, except in the case of a half-filled $4f$ shell, as implemented in Refs. [28,57]. In contrast, a smooth self-interaction process was achieved when we placed the $4f$ electrons in the core. Based on this observation, we speculate that the valence of Eu may not be entirely divalent, since Eu^{2+} should be adequately handled by the DFT calculations.

Since the failure to converge when considering the $4f$ states, we utilized the PAW pseudopotential Eu_2 to address this challenge, in which the spins of the $4f$ electrons are omitted. The resulting cell dimensions are: $a = 30.029$ Å, $b = 4.312$ Å, and $c = 11.628$ Å, which are slightly smaller than the experimental values. The band structure and density of states (DOS) are presented in Fig. 6. Although our calculations, without considering magnetism, may not fully reflect the actual electronic band structure of $Eu_{11}Zn_6As_{12}$, some insights can still be deduced. Firstly, the energy gap of $Eu_{11}Zn_6As_{12}$ is likely to be narrow and sensitive to the spin arrangement, explaining the reduced resistivity when a magnetic field is applied [20,58]. Secondly, the $4p$ orbitals of As dominate the states at the top of the valence band, owing to the absence of Eu $4f$ orbitals. Hybridization of As $4p$ and Eu $4f$ orbitals is common in Eu-based pnictides [21,28], making it reasonable to assume electron transfer between As $4p$ and Eu $4f$ orbitals, as discussed previously.

IV. CONCLUDING REMARKS

To summarize, the Eu-containing Zintl phase, $Eu_{11}Zn_6As_{12}$, was successfully synthesized and carefully characterized. $Eu_{11}Zn_6As_{12}$ exhibits unusual magnetic and transport properties, including complex magnetic behaviors, a large negative MR, and a nonlinear AHE. Essentially, $Eu_{11}Zn_6As_{12}$ is an antiferromagnet with uncompensated FM component. Three magnetic transitions are consistently

identified through the magnetization, specific heat, and resistivity measurements: FM fluctuations around 29 K (T_{F}), AFM ordering at 22 K (T_{N}), and an AFM-like transition at 9 K (T^*). The resistivity of $Eu_{11}Zn_6As_{12}$ is one order of magnitude higher than that of the isostructural compound $Eu_{11}Cd_6Sb_{12}$, and the strong FM fluctuations above T_{N} result in a prominent resistivity peak around 18 K. Moreover, a resistivity hysteresis is observed at low temperatures (<5 K) owing to the remnant FM component. The resistivity peak around T_{N} diminishes rapidly in increasing magnetic fields, leading to a maximum MR effect of -190% at 5 T. Our analysis of the field-dependent Hall resistivity suggests a carrier concentration of 1.2×10^{20} cm^{-3}, which may result from the commonly observed cation defects in Zintl phases or the mixed valence of Eu^{2+} and Eu^{3+}. A nonlinear AHE contribution occurs around T_{F} and T_{N}, similar to the cases in $CaAl_2Si_2$-type EuM_2X_2 compounds [15,17,48,49], which could be attributed to the nonzero spin chirality because of the noncollinear spins of Eu sites.

Our study demonstrates that the magnetism and charge transport properties of $Eu_{11}Zn_6As_{12}$ are distinct from those of other Eu-containing 11-6-12 phases, indicating that even sister materials with the same structure, specifically narrow-gap rare-earth Zintl phases, can exhibit substantially different physical properties. Therefore, the structural diversity of Zintl phases presents an exceptional platform for exploring the interplay between charge transport and magnetic ordering through tuning the composition. In addition, further experiments are required to elucidate the unusual properties of $Eu_{11}Zn_6As_{12}$, such as unraveling the complex spin structure and determining the true valence state of the Eu ions.

APPENDIX: MAGNETIZATION

Magnetization as a function of field $M(H)$, with fields applied along and perpendicular to the b axis, is shown in Figs. 7(a) and 7(b), indicating a weak magnetic anisotropy. As shown in Fig. 7(c), splittings in the ZFC and FC data are observed for both $H \parallel b$ and $H \perp b$.

[1] *Chemistry, Structure, and Bonding of Zintl Phases and Ions: Selected Topics and Recent Advances*, edited by S.M. Kauzlarich, 1st ed. (Wiley-VCH, New York, 1996).

[2] S. Fang, J. Li, K. Zou, H. Shuai, L. Xu, W. Deng, G. Zou, H. Hou, and X. Ji, Zintl chemistry: Current status and future perspectives, Chem. Eng. J. **433**, 133841 (2022).

[3] K. P. Devlin, N. Kazem, J. V. Zaikina, J. A. Cooley, J. R. Badger, J. C. Fettinger, V. Taufour, and S. M. Kauzlarich, $Eu_{11}Zn_4Sn_2As_{12}$: A ferromagnetic Zintl

semiconductor with a layered structure featuring extended Zn_4As_6 sheets and ethane-like Sn_2As_6 units, Chem. Mater. **30**, 7067 (2018).

[4] A. C. Payne, M. M. Olmstead, S. M. Kauzlarich, and D. J. Webb, Structure, magnetism, and magnetoresistance of the compounds $Eu_{14}MnAs_{11}$ and $Eu_{14}MnP_{11}$, Chem. Mater. **13**, 1398 (2001).

[5] J. Shuai, J. Mao, S. Song, Q. Zhang, G. Chen, and Z. Ren, Recent progress and future challenges on thermoelectric Zintl materials, Mater. Today Phys. **1**, 74 (2017).

[6] C. Chen, W. Xue, S. Li, Z. Zhang, X. Li, X. Wang, Y. Liu, J. Sui, X. Liu, F. Cao *et al.*, Zintl-phase Eu_2ZnSb_2: A promising thermoelectric material with ultralow thermal conductivity, Proc. Natl. Acad. Sci. USA **116**, 2831 (2019).

[7] W. Cao, H. Yang, Y. Li, C. Pei, Q. Wang, Y. Zhao, C. Li, M. Zhang, S. Zhu, J. Wu, L. Zhang, Z. Wang, Y. Yao, Z. Liu, Y. Chen, and Y. Qi, Pressure-induced superconductivity in the Zintl topological insulator $SrIn_2As_2$, Phys. Rev. B **108**, 224510 (2023).

[8] H. Li, S.-Y. Gao, S.-F. Duan, Y.-F. Xu, K.-J. Zhu, S.-J. Tian, J.-C. Gao, W.-H. Fan, Z.-C. Rao, J.-R. Huang, J.-J. Li, D.-Y. Yan, Z.-T. Liu, W.-L. Liu, Y.-B. Huang, Y.-L. Li, Y. Liu, G.-B. Zhang, P. Zhang, T. Kondo *et al.*, Dirac surface states in intrinsic magnetic topological insulators $EuSn_2As_2$ and $MnBi_{2n}Te_{3n+1}$, Phys. Rev. X **9**, 041039 (2019).

[9] H. Li, W. Gao, Z. Chen, W. Chu, Y. Nie, S. Ma, Y. Han, M. Wu, T. Li, Q. Niu, W. Ning, X. Zhu, and M. Tian, Magnetic properties of the layered magnetic topological insulator $EuSn_2As_2$, Phys. Rev. B **104**, 054435 (2021).

[10] M. Marshall, I. Pletikosić, M. Yahyavi, H.-J. Tien, T.-R. Chang, H. Cao, and W. Xie, Magnetic and electronic structures of antiferromagnetic topological material candidate $EuMg_2Bi_2$, J. Appl. Phys. **129**, 035106 (2021).

[11] Y. Xu, Z. Song, Z. Wang, H. Weng, and X. Dai, Higher-order topology of the axion insulator $EuIn_2As_2$, Phys. Rev. Lett. **122**, 256402 (2019).

[12] Y. Zhang, K. Deng, X. Zhang, M. Wang, Y. Wang, C. Liu, J.-W. Mei, S. Kumar, E. F. Schwier, K. Shimada, C. Chen, and B. Shen, In-plane antiferromagnetic moments and magnetic polaron in the axion topological insulator candidate $EuIn_2As_2$, Phys. Rev. B **101**, 205126 (2020).

[13] G. Hua, S. Nie, Z. Song, R. Yu, G. Xu, and K. Yao, Dirac semimetal in type-IV magnetic space groups, Phys. Rev. B **98**, 201116(R) (2018).

[14] J.-Z. Ma, S. M. Nie, C. J. Yi, J. Jandke, T. Shang, M. Y. Yao, M. Naamneh, L. Q. Yan, Y. Sun, A. Chikina *et al.*, Spin fluctuation induced Weyl semimetal state in the paramagnetic phase of $EuCd_2As_2$, Sci. Adv. **5**, eaaw4718 (2019).

[15] Y. Xu, L. Das, J. Z. Ma, C. J. Yi, S. M. Nie, Y. G. Shi, A. Tiwari, S. S. Tsirkin, T. Neupert, M. Medarde, M. Shi, J. Chang, and T. Shang, Unconventional transverse transport above and below the magnetic transition temperature in Weyl semimetal $EuCd_2As_2$, Phys. Rev. Lett. **126**, 076602 (2021).

[16] P. Rosa, Y. Xu, M. Rahn, J. Souza, S. Kushwaha, L. Veiga, A. Bombardi, S. Thomas, M. Janoschek, E. Bauer *et al.*, Colossal magnetoresistance in a nonsymmorphic antiferromagnetic insulator, npj Quantum Mater. **5**, 52 (2020).

[17] Z.-C. Wang, J. D. Rogers, X. Yao, R. Nichols, K. Atay, B. Xu, J. Franklin, I. Sochnikov, P. J. Ryan, D. Haskel, and F. Tafti, Colossal magnetoresistance without mixed valence in a layered phosphide crystal, Adv. Mater. **33**, 2005755 (2021).

[18] Z.-C. Wang, E. Been, J. Gaudet, G. M. A. Alqasseri, K. Fruhling, X. Yao, U. Stuhr, Q. Zhu, Z. Ren, Y. Cui, C. Jia, B. Moritz, S. Chowdhury, T. Devereaux, and F. Tafti, Anisotropy of the magnetic and transport properties of $EuZn_2As_2$, Phys. Rev. B **105**, 165122 (2022).

[19] T. Berry, V. J. Stewart, B. W. Y. Redemann, C. Lygouras, N. Varnava, D. Vanderbilt, and T. M. McQueen, A-type antiferromagnetic order in the Zintl-phase insulator $EuZn_2P_2$, Phys. Rev. B **106**, 054420 (2022).

[20] K. Singh, S. Dan, A. Ptok, T. A. Zaleski, O. Pavlosiuk, P. Wiśniewski, and D. Kaczorowski, Superexchange interaction in insulating $EuZn_2As_2$, Phys. Rev. B **108**, 054402 (2023).

[21] L.-L. Wang, N. H. Jo, B. Kuthanazhi, Y. Wu, R. J. McQueeney, A. Kaminski, and P. C. Canfield, Single pair of Weyl fermions in the half-metallic semimetal $EuCd_2As_2$, Phys. Rev. B **99**, 245147 (2019).

[22] M. C. Rahn, J.-R. Soh, S. Francoual, L. S. I. Veiga, J. Strempfer, J. Mardegan, D. Y. Yan, Y. F. Guo, Y. G. Shi, and A. T. Boothroyd, Coupling of magnetic order and charge transport in the candidate Dirac semimetal $EuCd_2As_2$, Phys. Rev. B **97**, 214422 (2018).

[23] V. Sunko, Y. Sun, M. Vranas, C. C. Homes, C. Lee, E. Donoway, Z.-C. Wang, S. Balguri, M. B. Mahendru, A. Ruiz, B. Gunn, R. Basak, S. Blanco-Canosa, E. Schierle, E. Weschke, F. Tafti, A. Frano, and J. Orenstein, Spin-carrier coupling induced ferromagnetism and giant resistivity peak in $EuCd_2P_2$, Phys. Rev. B **107**, 144404 (2023).

[24] C. C. Homes, Z.-C. Wang, K. Fruhling, and F. Tafti, Optical properties and carrier localization in the layered phosphide $EuCd_2P_2$, Phys. Rev. B **107**, 045106 (2023).

[25] X. Chen, W. Yang, J.-Y. Lu, Z. Zhou, Z. Ren, G.-H. Cao, S. Dong, and Z.-C. Wang, Carrier-induced transition from antiferromagnetic insulator to ferromagnetic metal in the layered phosphide $EuZn_2P_2$, Phys. Rev. B **109**, L180410 (2024).

[26] N. H. Jo, B. Kuthanazhi, Y. Wu, E. Timmons, T.-H. Kim, L. Zhou, L.-L. Wang, B. G. Ueland, A. Palasyuk, D. H. Ryan, R. J. McQueeney, K. Lee, B. Schrunk, A. A. Burkov, R. Prozorov, S. L. Bud'ko, A. Kaminski, and P. C. Canfield, Manipulating magnetism in the topological semimetal $EuCd_2As_2$, Phys. Rev. B **101**, 140402(R) (2020).

[27] S. Roychowdhury, M. Yao, K. Samanta, S. Bae, D. Chen, S. Ju, A. Raghavan, N. Kumar, P. Constantinou, S. N. Guin *et al.*, Anomalous Hall conductivity and nernst effect of the ideal Weyl semimetallic ferromagnet $EuCd_2As_2$, Adv. Sci. **10**, 2207121 (2023).

[28] X. Chen, Z. Wang, Z. Zhou, W. Yang, Y. Liu, J.-Y. Lu, Z. Ren, G.-H. Cao, F. Tafti, S. Dong, and Z.-C. Wang, Manipulating magnetism and transport properties of $EuCd_2P_2$ with a low carrier concentration, Phys. Rev. B **109**, 224428 (2024).

[29] B. Saparov and S. Bobev, Undecaeuropium hexazinc dodecaarsenide, Acta Crystallogr. Sect. E **66**, i24 (2010).

[30] B. Saparov, S. Bobev, A. Ozbay, and E. R. Nowak, Synthesis, structure and physical properties of the new Zintl phases $Eu_{11}Zn_6Sb_{12}$ and $Eu_{11}Cd_6Sb_{12}$, J. Solid State Chem. **181**, 2690 (2008).

[31] O. V. Dolomanov, L. J. Bourhis, R. J. Gildea, J. A. Howard, and H. Puschmann, OLEX2: A complete structure solution, refinement and analysis program, J. Appl. Crystallogr. **42**, 339 (2009).

[32] C. B. Hübschle, G. M. Sheldrick, and B. Dittrich, ShelXle: A Qt graphical user interface for SHELXL, J. Appl. Crystallogr. **44**, 1281 (2011).

[33] K. Momma and F. Izumi, *VESTA* 3 for three-dimensional visualization of crystal, volumetric and morphology data, J. Appl. Crystallogr. **44**, 1272 (2011).

[34] G. Kresse and J. Furthmüller, Efficient iterative schemes for ab initio total-energy calculations using a plane-wave basis set, Phys. Rev. B **54**, 11169 (1996).

[35] P. E. Blöchl, Projector augmented-wave method, Phys. Rev. B **50**, 17953 (1994).

[36] J. P. Perdew, K. Burke, and M. Ernzerhof, Generalized gradient approximation made simple, Phys. Rev. Lett. **77**, 3865 (1996).

[37] J. Wang, M. Yang, M.-Y. Pan, S.-Q. Xia, X.-T. Tao, H. He, G. Darone, and S. Bobev, Synthesis, crystal and electronic structures, and properties of the new pnictide semiconductors $A_2 CdPn_2$ (A = Ca, Sr, Ba, Eu; Pn = P, As), Inorg. Chem. **50**, 8020 (2011).

[38] J. Wang, S.-Q. Xia, X.-T. Tao, M. C. Schäfer, and S. Bobev, New ternary phosphides and arsenides. Syntheses, crystal structures, physical properties of Eu_2ZnP_2, $Eu_2Zn_2P_3$ and $Eu_2Cd_2As_3$, J. Solid State Chem. **205**, 116 (2013).

[39] M. Bałanda, AC susceptibility studies of phase transitions and magnetic relaxation: Conventional, molecular and low-dimensional magnets, Acta Phys. Pol. A **124**, 964 (2013).

[40] L. de Jongh and A. Miedema, Experiments on simple magnetic model systems, Adv. Phys. **23**, 1 (1974).

[41] S. J. Sebastian, K. Somesh, M. Nandi, N. Ahmed, P. Bag, M. Baenitz, B. Koo, J. Sichelschmidt, A. A. Tsirlin, Y. Furukawa, and R. Nath, Quasi-one-dimensional magnetism in the spin-$\frac{1}{2}$ antiferromagnet $BaNa_2Cu(VO_4)_2$, Phys. Rev. B **103**, 064413 (2021).

[42] Z.-C. Wang, Y.-T. Shao, Y.-Q. Lin, S.-J. Song, B.-Z. Li, E.-J. Cheng, S.-Y. Li, Q.-Q. Zhu, Z. Ren, and G.-H. Cao, Absence of superconductivity in electron-doped chromium pnictides $ThCrAsN_{1-x}O_x$, Phys. Rev. B **108**, 064503 (2023).

[43] D. C. Johnston, Magnetic dipole interactions in crystals, Phys. Rev. B **93**, 014421 (2016).

[44] S. Pakhira, M. A. Tanatar, and D. C. Johnston, Magnetic, thermal, and electronic-transport properties of $EuMg_2Bi_2$ single crystals, Phys. Rev. B **101**, 214407 (2020).

[45] M. E. Fisher, Relation between the specific heat and susceptibility of an antiferromagnet, Philos. Mag. **7**, 1731 (1962).

[46] D. C. Johnston, Unified molecular field theory for collinear and noncollinear Heisenberg antiferromagnets, Phys. Rev. B **91**, 064427 (2015).

[47] X. Cao, J.-X. Yu, P. Leng, C. Yi, X. Chen, Y. Yang, S. Liu, L. Kong, Z. Li, X. Dong, Y. Shi, M. Bibes, R. Peng, J. Zang, and F. Xiu, Giant nonlinear anomalous Hall effect induced by spin-dependent band structure evolution, Phys. Rev. Res. **4**, 023100 (2022).

[48] K. Singh, O. Pavlosiuk, S. Dan, D. Kaczorowski, and P. Wiśniewski, Large unconventional anomalous Hall effect arising from spin chirality within domain walls of an antiferromagnet $EuZn_2Sb_2$, Phys. Rev. B **109**, 125107 (2024).

[49] E. Yi, D. F. Zheng, F. Pan, H. Zhang, B. Wang, B. Chen, D. Wu, H. Liang, Z. X. Mei, H. Wu, S. A. Yang, P. Cheng, M. Wang, and B. Shen, Topological Hall effect driven by short-range magnetic order in $EuZn_2As_2$, Phys. Rev. B **107**, 035142 (2023).

[50] G. S. Pomrehn, A. Zevalkink, W. G. Zeier, A. van de Walle, and G. J. Snyder, Defect-controlled electronic properties in AZn_2Sb_2 zintl phases, Angew. Chem. Int. Ed. **53**, 3422 (2014).

[51] E. S. Toberer, A. F. May, B. C. Melot, E. Flage-Larsen, and G. J. Snyder, Electronic structure and transport in thermoelectric compounds AZn_2Sb_2 (A = Sr, Ca, Yb, Eu), Dalton Trans. **39**, 1046 (2010).

[52] P. Gorai, A. Goyal, E. S. Toberer, and V. Stevanović, A simple chemical guide for finding novel *n*-type dopable Zintl pnictide thermoelectric materials, J. Mater. Chem. A **7**, 19385 (2019).

[53] S.-Q. Xia and S. Bobev, Are $Ba_{11}Cd_6Sb_{12}$ and $Sr_{11}Cd_6Sb_{12}$ Zintl phases or not? A density-functional theory study, J. Comput. Chem. **29**, 2125 (2008).

[54] S. Danzenbächer, D. V. Vyalikh, Y. Kucherenko, A. Kade, C. Laubschat, N. Caroca-Canales, C. Krellner, C. Geibel, A. V. Fedorov, D. S. Dessau, R. Follath, W. Eberhardt, and S. L. Molodtsov, Hybridization phenomena in nearly-half-filled f-shell electron systems: Photoemission study of $EuNi_2P_2$, Phys. Rev. Lett. **102**, 026403 (2009).

[55] F. Ronning, E. D. Bauer, T. Park, S.-H. Baek, H. Sakai, and J. D. Thompson, Superconductivity and the effects of pressure and structure in single-crystalline $SrNi_2P_2$, Phys. Rev. B **79**, 134507 (2009).

[56] T. Mine, H. Yanagi, T. Kamiya, Y. Kamihara, M. Hirano, and H. Hosono, Nickel-based phosphide superconductor with infinite-layer structure, $BaNi_2P_2$, Solid State Commun. **147**, 111 (2008).

[57] X. Yang and S. Dong, Oxidation tuning of ferroic transitions in Gd_2C monolayer, J. Chem. Phys. **160**, 014705 (2024).

[58] G. Cuono, R. M. Sattigeri, C. Autieri, and T. Dietl, *Ab initio* overestimation of the topological region in Eu-based compounds, Phys. Rev. B **108**, 075150 (2023).